Observation of Free-Boundary-Induced Chiral Anomaly Bulk States in Elastic Twisted Kagome Metamaterials

Zi-Dong Zhang,[1] Ming-Hui Lu,[1,2,*] and Yan-Feng Chen[1,2,†]
[1]National Laboratory of Solid State Microstructures & Department of Materials Science and Engineering, Nanjing University, Nanjing 210093, China
[2]Jiangsu Key Laboratory of Artificial Functional Materials, Nanjing University, Nanjing 210093, China

(Received 6 July 2023; accepted 22 December 2023; published 22 February 2024)

Chiral anomaly bulk states (CABSs) can be realized by choosing appropriate boundary conditions in a finite-size waveguide composed of two-dimensional Dirac semimetals, which have unidirectional and robust transport similar to that of valley edge states. CABSs use almost all available guiding space, which greatly improves the utilization of metamaterials. Here, free-boundary-induced CABSs in elastic twisted kagome metamaterials with C_{3v} symmetry are experimentally confirmed. The robust valley-locked transport and complete valley state conversion are experimentally observed. Importantly, the sign of the group velocity near the K and K' points can be reversed by suspending masses at the boundary to manipulate the onsite potential. Moreover, CABSs are demonstrated in nanoelectromechanical phononic crystals by constructing an impedance-mismatched hard boundary. These results open new possibilities for designing more compact, space-efficient, and robust elastic wave macro- and microfunctional devices.

DOI: 10.1103/PhysRevLett.132.086302

Topological acoustics, which enables robust sound wave transmission and localization, is revolutionizing the design of acoustic devices [1–3]. Acoustic topological insulators are synthetic materials with a gapped bulk energy spectrum and protected in-gap chiral states. To date, the most basic application is to construct topological edge states according to the bulk-edge correspondence [4–7]. The most common method is to create the boundary of two crystals that carry different topological invariants [4–7]. The topological mode only exists at the structural boundary, so most of the footprint of the structure is unused. It is worth considering whether or not robust bulk states can be achieved. In a three-dimensional (3D) Weyl semimetal, there are chiral anomaly zeroth Landau levels equivalent to CABSs [8–15]. The mode is a bulk state, and the one-way transmission of the chiral Landau mode can overcome the energy loss caused by backscattering [14–17]. Various electronic and photonic systems that support chiral anomaly zeroth Landau levels have been confirmed [14,15].

The Weyl point corresponds to the Dirac point of the two-dimensional (2D) system. Discrete Landau levels can also be achieved by introducing artificially synthesized magnetic fields in 2D Dirac semimetals such as electromagnetic systems [18], aeroacoustics [19,20], and elastic wave systems [21]. The artificial magnetic field is generated by applying an external stress or introducing a uniaxial deformation. However, the corresponding zeroth Landau mode can only achieve bulk states in the flat band domain and is still an edge mode in the dispersion domain [21]. Recently, CABSs have been achieved in 2D Dirac semimetal materials with a suitable choice of periodic boundary conditions due to the finite size effect [22,23]. 2D CABSs have unidirectional and robust transport similar to that of valley-protected edge state transport [5,24,25]. Compared to the edge state, the mode is transmitted in the bulk and not localized at the boundary or domain wall. CABSs use almost all available boot space and greatly improve the space utilization. However, CABSs in elastic waves have not been explored. Elastic waves in solids have anti-jamming capability, extremely low losses, and scalability toward integrated devices. CABSs in elastic waves enable more compact, space-efficient, and robust phonon waveguides, which will undoubtedly play an important role in advanced information manipulation [26–30].

In this letter, we realize CABSs by configuring free boundaries in a finite-sized waveguide in the elastic kagome lattice with C_{3v} symmetry. The bulk state has a valley-locked property, which can be inverted by changing the boundary configuration of the waveguide. Elastic CABSs have the following major distinct characteristics from those in the air [22]: (i) The bands are selectively prohibited based on the compatibility of vibration modes with free boundaries; (ii) CABSs are realized in lattices with C_{3v} symmetry. When the symmetry is reduced from C_{6v} to C_{3v}, this system can directly achieve complete valley conversion of CABS without modifying the waveguide. (iii) We propose a method to regulate the boundary potential, i.e., adding suspension on the boundary, to manipulate the group velocity of the CABS. Finally, we theoretically propose that CABSs can be achieved in nanoelectromechanical systems by constructing impedance-mismatched hard boundaries.

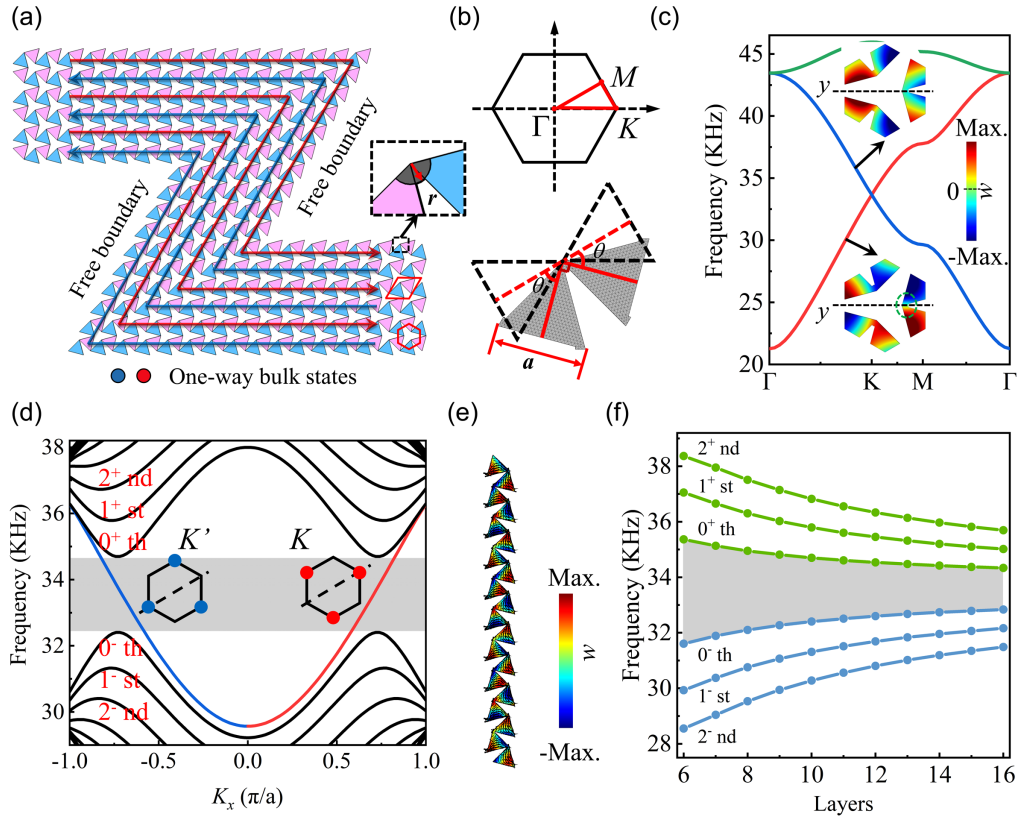

FIG. 1. (a) Schematic diagram to implement CABSs in a continuous elastic body. The red boxes are two types of unit cells. (b) Upper panel: the first Brillouin zone of the PnCs. Lower panel: the twist angle. (c) Band diagram of an out-of-plane elastic wave. The inset images show the eigenstates, where the color bar is out-of-plane displacements (w). The blue band and the red band correspond to an even mode and an odd mode with a mirror-y parity, respectively. (d) Projected band of the PnCs waveguides, which is a free boundary in the y direction, and periodic boundary condition in the x direction. The pseudogap (shadow region) is caused by the finite width of the PnC waveguide. The PnCs waveguides have 10 layers, and the thickness of each layer is $(\sqrt{6}/2)a$. (e) w field of CABSs. Arrows show energy flux fields. (f) The bandwidth of CABS varies with the number of layers in PnCs waveguide. Because CABS exists in the entire pseudogap, the pseudogap bandwidth is equivalent to the operating bandwidth of CABS.

Figure 1(a) shows the implementation of CABSs in elastic twisted kagome lattices (TKLs) with C_{3v} symmetry. TKLs with easy preparation and adjustability are chosen for verification [31–37]. A TKL comprises two 90°-rotated equilateral triangles with side length $\boldsymbol{a} = 13.5$ mm, where the triangles are elastic domains [Fig. 1(b)] [35]. The lower panel of Fig. 1(b) shows the twist angle in TKLs. To realize kagome lattices in continuous elastomers, ligaments are used to replace the hinges. The ligaments are constructed as a sector with radius $\boldsymbol{r} = 1.5$ mm. Then, the structure is prepared on a 1.5-mm-thick aluminum plate. Figure 1(c) shows the band curves of the structure, and only out-of-plane elastic waves are concerned (Fig. S1 shows the band including all modes [38]). The metamaterial is a 2D Dirac semimetal material, which forms a degeneracy point at point K. Then, this 2D Dirac semimetal is constructed into a finite-size waveguide. Because of finite size effects, the pseudo-gap is formed. Next, the suitable boundary configuration is selected to realize the one-way robust transmission of the valley-locked chiral bulk states near the Dirac point. A Dirac-like Hamiltonian of a waveguide with thickness L can be expressed as $H(y) = \sigma_x k_x v_D - i\partial_y \sigma_y v_D + m(y)\sigma_z$ [22]. The boundary causes a step mass term near the Diarc point, $m(y) = m_1, y < 0; 0, 0 \le y \le L; m_2, y > L$. The Hamiltonian has a bulk mirror-y symmetry in the domain $0 \le y \le L$, $\sigma_x H(y)\sigma_x = H(-y)$. Hence, the eigensolutions at the Dirac point [22] are

$$\psi = \begin{cases} e^{|m_1|y}\begin{pmatrix} 1 \\ \mathrm{sgn}(m_1) \end{pmatrix} & y \le 0 \\ \begin{pmatrix} 1 \\ \pm 1 \end{pmatrix} & 0 \le y \le L. \\ e^{-|m_2|(y-L)}\begin{pmatrix} 1 \\ -\mathrm{sgn}(m_2) \end{pmatrix} & y \ge L \end{cases} \quad (1)$$

The mass terms introduce an exponentially decaying solution and hence form a gap, i.e., the finite size effects. When $m_1 > 0$ and $m_2 < 0$, the bulk even mode $\psi = \binom{1}{1}$ with a certain mirror-y parity is confined in the middle

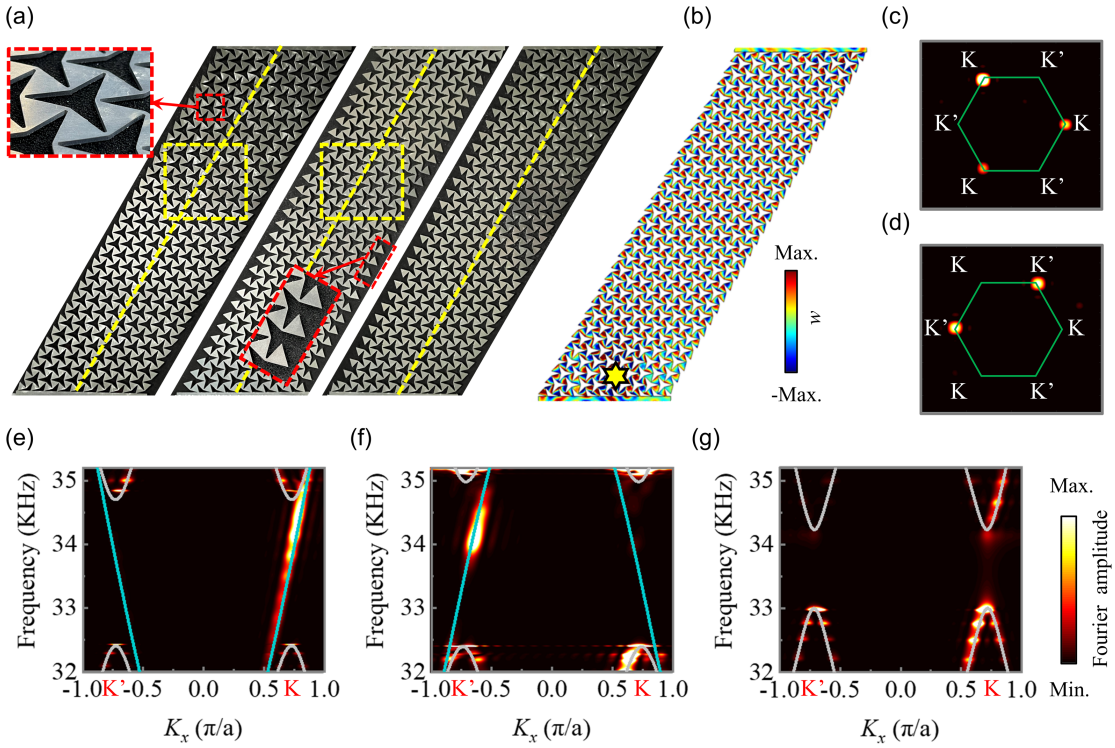

FIG. 2. (a) Experimental sample of the 10-layer unmodified waveguides, waveguides with suspended masses on both sides and waveguides with a suspended mass on one side from left to right, respectively. Inset: partially enlarged view of the structure. (b) w distributions at 34.2 kHz excited by a point source (yellow star). (c),(d) Fourier spectra for the 10-layer waveguides and waveguides with suspended masses on both sides, respectively, which are obtained by w in the dotted box in (a). (e)–(g) Experimentally tested projected bands correspond to the three waveguides in (a), which are obtained by a Fourier transformation of the measured field distribution interval with a lattice period along the yellow dotted line in (a). The solid line in figure is the calculated band curve.

domain. Otherwise, the bulk odd mode $\psi = \binom{1}{-1}$ is supported.

In elastomers, fixed boundaries that are similar to hard boundaries in air [22] can introduce CABSs, as shown in Fig. S2 [38]. However, implementing fixed boundaries through clamping is an energy-consuming method that increases the transmission loss of elastic waves. Here, we adopt a more convenient and adjustable free boundary. Because the free boundary cannot guarantee that the displacement field at the waveguide boundary [marked by the blue dotted circle in Fig. 1(c)] is always 0 during propagation of the elastic wave, this boundary is incompatible with the red band of Fig. 1(c), which makes it prohibited (see movie S1 [38]). The vibrational mode of the blue band is compatible with the free boundary and is supported (see movie S2 [38]). It corresponds to $m_1 = m_2 = +\infty$, so the even bulk mode is excited. Hence, when a finite-size waveguide with free-boundary conditions on both sides is constructed, CABSs appear in the pseudogap in the projected band [Fig. 1(d)]. The chirality is different from the chiral elastic wave substituted by the intrinsic spin angular momentum [41]. This method can also be used for elastic wave systems with C_{6v} symmetry [Fig. S3 [38]]. These states are bulk states, not boundary states, and their out-of-plane displacement fields are uniformly distributed throughout the waveguide [Fig. 1(e)]. CABSs have K or K' valley locked in the pseudo-band gap, where the blue and red bands correspond to different valley polarizations in Fig. 1(d).

The slope (the sign of the group velocity) of the CABS depends on the selection of valley, where the K or K' valley corresponds to the opposite mass terms and supports the opposite bulk mode, as shown in Eq. (1). The slope of the CABS near points K and K' cannot be reversed by changing the number of waveguide layers [Fig. 1(f)] and cutting boundaries (Fig. S4 [38]) in the TKL, which is different from the C_{6v} system [22]. When the number of waveguide layers increases, the pseudogap decreases (the operating bandwidth of CABS decreases), as shown in Fig. 1(f). Here, we select different valleys by adjusting the boundary potential, i.e., hanging a mass at the boundary. By regulating the boundary potential, the mass term can be changed, which enables the waveguide to support the opposite vibration mode and ultimately reverses the valley polarization, as shown in Fig. S5(e) and movie S3 [38]. Different shapes and sizes of suspensions can be used to adjust the boundary potential (Figs. S6–S7). Interestingly, when $|m_1| \neq |m_2|$, both odd and even modes are prohibited,

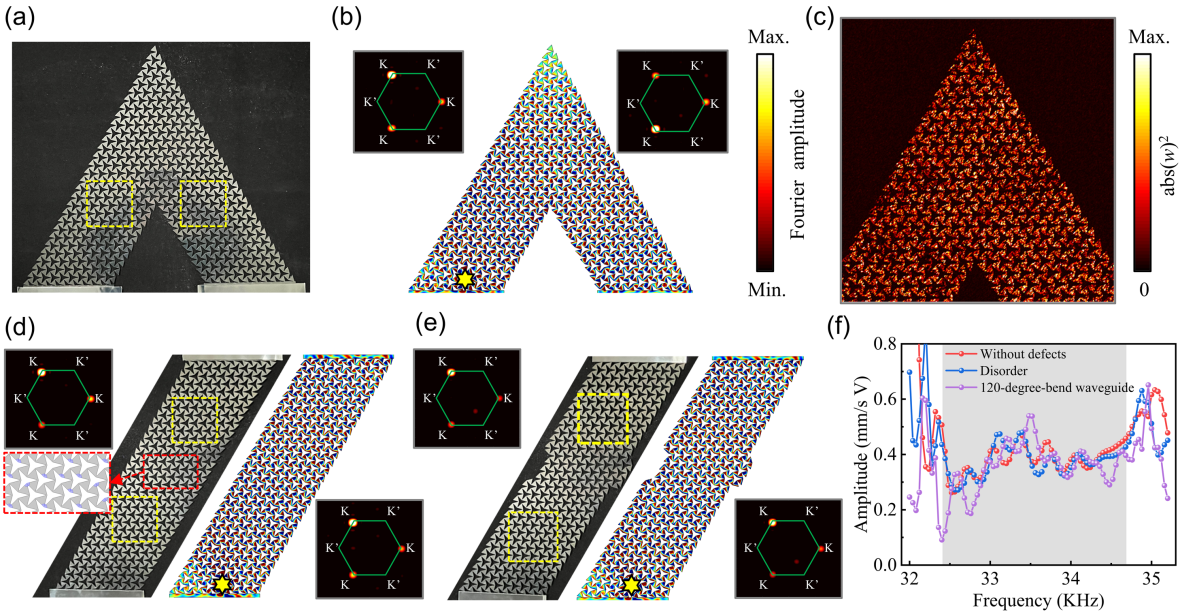

FIG. 3. (a) Photo of the PnCs waveguides with a 120° bend. (b) Simulated w distributions at 34.2 kHz for a point source (yellow star) on the 120°-bend waveguides. (c) Experimental w distributions at 34.2 kHz for a point source on the 120°-bend waveguides. (d) Photo of the disordered waveguides (left panel) and w distributions (34.2 kHz) on the disordered waveguides (right panel). The distortion is marked in the red dotted box. (e) Photo of the defective waveguides (left panel) and w distributions (34.2 kHz) on the defective waveguides (right panel). (f) Transmission curves of the 120-degree-bend waveguides and the disordered waveguides are compared with those of the waveguide with no defects. Inset picture of (b), (c), and (e): Corresponding Fourier spectra in the dashed rectangle.

so a forbidden band is formed near the Dirac point [Fig. S5(f)]. The twist angle only affects the operating frequency of CABS, as shown in Figs. S8 and S9 [38].

To observe CABSs and the effect of the onsite potential on CABSs in elastic twisted kagome metamaterials, we construct related experimental samples, as shown in Fig. 2(a). These samples are prepared by laser cutting and subsequently mechanically flattened. After the elastic wave excited by the point source propagates through several lattices, the wave is evenly distributed in the entire waveguide [Fig. 2(b)]. Therefore, the bulk states use almost all of the available guiding space. The unmodified waveguides and two-sided-suspended-mass waveguides have opposite valley polarization characteristics. Only the states near the K valley for the 10-layer waveguides [Fig. 2(c)] are detected in the experiment, which indicates the excitation of CABSs locked at the K valleys. However, only the states near the K' valley are tested in the waveguide suspended mass on both sides, as shown in Fig. 2(d). The valley characteristics of CABSs can be experimentally reversed by modifying the onsite potential of the waveguide boundary. The projected bands that correspond to the three waveguides are experimentally obtained, as shown in Figs. 2(e)–2(g). The 10-layer waveguides and two-sided-suspended-mass waveguides with K valley or K' valley are locked in the pseudogap, respectively. Figure 2(g) shows that a pseudogap can be generated by suspending the mass on one side of the waveguide. These results provide new methods to control the chirality of CABSs and generate a complete bandgap.

Because of the valley-locked property of CABSs, the chiral bulk states have immunity against sharp bends, distortions, or defects. To verify the robustness, the PnCs waveguides with a 120° bend, disorders, and defects are fabricated, as shown in Figs. 3(a)–3(e). The elastic wave excited by the point source extends to the entire waveguide space, there is almost no energy loss, and the waveform does not undergo obvious distortion when the wave passes through the bending, twisting, and defect regions, as shown in Figs. 3(b), 3(c), and 3(e), respectively. CABSs are immune to different types of defects, as shown in Fig. S10 [38]. The Fourier transform before and after the turning, distortions, and defects is used to obtain the momentum space information, as shown in the inset of Figs. 3(b)–3(e). Both domains of the 120° bend waveguides have identical valley characteristics, which enable the wave to turn. When the wave passes through the distortions and defects, the wave has the characteristic of K valley locking, so the intervalley that scatters from valley K valley to valley K' is weak; thus, the states are robust. As shown in the displacement field obtained through simulation in Fig. 3(d), the wave can pass through the 120° bend and is evenly distributed in the entire waveguide space with almost no loss of energy. The good consistency in the transmission curves [Fig. 3(f)] indicates the immunity of CABSs against bends, disorders, and defects.

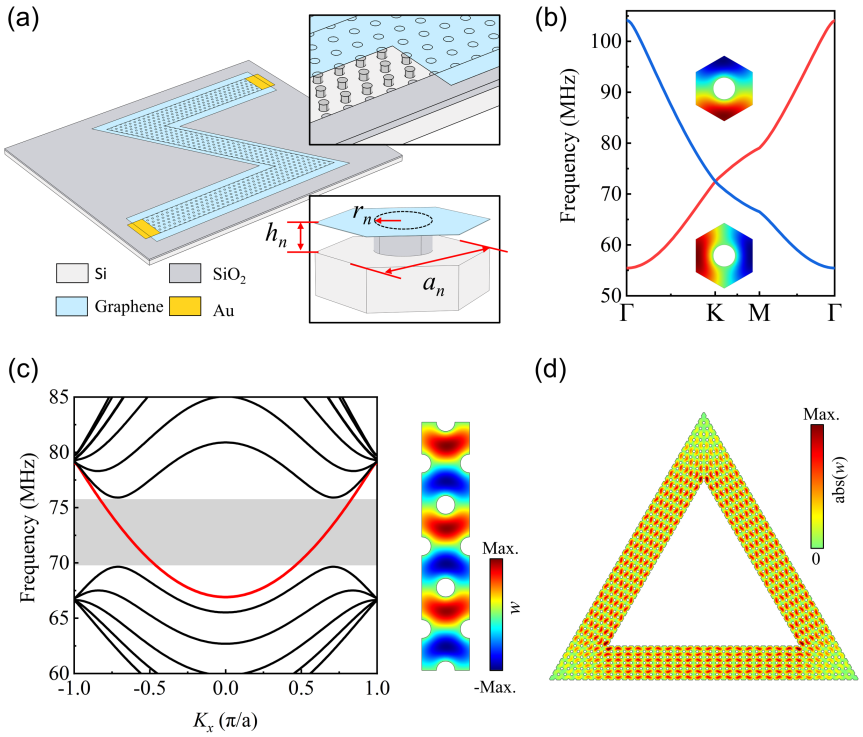

FIG. 4. (a) Schematic diagram of the implementation of CABSs in nanoelectromechanical systems, which incorporate a dual 120°-bend waveguide. Its lattice constant a_n is $6\sqrt{3}$ um, the circular rods' diameter r_n is 4 um, and the micropillar height h_n is 200 nm. (b) Band diagram. The inset images are the eigenstates. (c) Projected band of the PnCs waveguides. w of the CABSs (right panel). The PnCs waveguides have six layers. (d) w of the triangular waveguide resonator at 72.457 MHz.

Compared to the C_{6v} symmetry in air, the twisted kagome metamaterials with C_{3v} symmetry (threefold rotational symmetry) can achieve the complete valley conversion of CABSs without modifying the waveguide [22]. The 60°-bend waveguides were prepared for verification [Fig. S11(a)]. The wave excited at the Dirac point frequency is evenly distributed in the waveguide space after it has propagated through several lattices, and the wave can also smoothly pass through the 60° turn [Fig. S11(b)]. Figure S11(c) shows the experimental displacement field distribution. Then, Figs. S11(d) and S11(e) show its momentum space information. Figures S11(f) and S11(g) show the corresponding projected bands along the X and X' directions. The experimentally tested transmission curves [Fig. S11(h)] show that the conversion characteristics can be realized in the pseudogap. These results confirm that CABSs transform the valley polarization characteristics after the wave passes through a 60° turn. The complete valley conversion has potential applications in valley information transforms [38].

As discussed above, we have realized CABSs in the macroscopic elastic wave system. However, it is difficult to realize such a large-area suspended structure in on-chip elastic wave systems. In nanoelectromechanical systems, acoustic impedance-mismatched boundaries, similar to that of hard boundaries in air acoustics, can be constructed to achieve CABSs [42–47]. Figure 4(a) shows the nanoelectromechanical PnCs structures, where single-layer graphene is pinned on micropillar arrays with triangular lattices. Because of the acoustic impedance mismatch between the waveguide and its unsuspended bulklike environment, acoustic energy can be confined to the waveguide [45,46]. Figure 4(b) shows the corresponding band diagram of the structure. The detailed process of numerical calculation is shown in Fig. S12 [38]. The quasihard boundary condition is incompatible with the vibration mode of the red band [Fig. 4(b)], which is prohibited. Then, CABSs can also be generated in the pseudogap in Fig. 4(c), and Fig. S13(a) demonstrates the robust waveguides. Through the characteristics of CABSs, we design a triangular resonator, as shown in Fig. 4(e). Figure S13(b) shows the eigenstates of the triangular resonator, and Fig. S14 shows the realized electrically tunable narrow-band switch [38].

In conclusion, we realize CABSs by configuring free boundaries in a finite-sized waveguide in the elastic kagome lattice with C_{3v} symmetry. We demonstrate that the bulk state has a valley-locked property, and the inversion of the valley-locked property can be achieved by changing the boundary configuration of the waveguide. Then, the states are immune to sharp bends, structural distortions, and structural defects due to the valley-locked feature. Since the twisted kagome lattice has C_{3v} symmetry, the waveguide can completely convert the valley state from

K to K'. We theoretically propose that CABSs can be achieved in nanoelectromechanical systems by constructing impedance-mismatched hard boundaries. These results open new possibilities for designing more compact, space-efficient, and robust elastic wave macro- and microfunctional devices, such as large-area elastic waveguides, high-quality factor elastic wave resonators, elastic wave focusing, phonon lasers, etc.

We acknowledge Bi-Ye Xie for fruitful discussions. The work is jointly supported by the National Key R&D Program of China (Grants No. 2021YFB3801801, No. 2023YFA1406904, No. 2022YFA1404404), and the National Natural Science Foundation of China (Grants No. 11890702, No. 52250363). Z.-D. Z. acknowledges support from the China Postdoctoral Science Foundation (2022M711571).

*luminghui@nju.edu.cn
†yfchen@nju.edu.cn

[1] X. Zhang, F. Zangeneh-Nejad, Z. G. Chen, M. H. Lu, and J. Christensen, A second wave of topological phenomena in photonics and acoustics, Nature (London) **618**, 687 (2023).
[2] H. Xue, Y. Yang, and B. Zhang, Topological acoustics, Nat. Rev. Mater. **7**, 974 (2022).
[3] S. D. Huber, Topological mechanics, Nat. Phys. **12**, 621 (2016).
[4] M. Xiao, G. Ma, Z. Yang, P. Sheng, Z. Q. Zhang, and C. T. Chan, Geometric phase and band inversion in periodic acoustic systems, Nat. Phys. **11**, 240 (2015).
[5] J. Lu, C. Qiu, L. Ye, X. Fan, M. Ke, F. Zhang, and Z. Liu, Observation of topological valley transport of sound in sonic crystals, Nat. Phys. **13**, 369 (2017).
[6] S. H. Mousavi, A. B. Khanikaev, and Z. Wang, Topologically protected elastic waves in phononic metamaterials, Nat. Commun. **6**, 8682 (2015).
[7] C. He, X. Ni, H. Ge, X. C. Sun, Y. B. Chen, M. H. Lu, X. P. Liu, and Y. F. Chen, Acoustic topological insulator and robust one-way sound transport, Nat. Phys. **12**, 1124 (2016).
[8] Z. K. Liu, B. Zhou, Y. Zhang, Z. J. Wang, H. M. Weng, D. Prabhakaran, S.-K. Mo, Z. X. Shen, Z. Fang, X. Dai, Z. Hussain, and Y. L. Chen, Discovery of a three-dimensional topological Dirac semimetal, Na3Bi, Science **343**, 864 (2014).
[9] X. Wan, A. M. Turner, A. Vishwanath, and S. Y. Savrasov, Topological semimetal and Fermi-arc surface states in the electronic structure of pyrochlore iridates, Phys. Rev. B **83**, 205101 (2011).
[10] L. Lu, L. Fu, J. D. Joannopoulos, and M. Soljačić, Weyl points and line nodes in gyroid photonic crystals, Nat. Photonics **7**, 294 (2013).
[11] L. Lu, Z. Wang, D. Ye, L. Ran, L. Fu, J. D. Joannopoulos, and M. Soljačić, Experimental observation of Weyl points, Science **349**, 622 (2015).
[12] H. He, C. Qiu, L. Ye, X. Cai, X. Fan, M. Ke, F. Zhang, and Z. Liu, Topological negative refraction of surface acoustic waves in a Weyl phononic crystal, Nature (London) **560**, 61 (2018).
[13] F. Li, X. Huang, J. Lu, J. Ma, and Z. Liu, Weyl points and Fermi arcs in a chiral phononic crystal, Nat. Phys. **14**, 30 (2018).
[14] C. Zhang, E. Zhang, W. Wang, Y. Liu, Z.-G. Chen, S. Lu, S. Liang, J. Cao, X. Yuan, L. Tang, Q. Li, C. Zhou, T. Gu, Y. Wu, J. Zou, and F. Xiu, Room-temperature chiral charge pumping in Dirac semimetals, Nat. Commun. **8**, 13741 (2017).
[15] H. Jia, R. Zhang, W. Gao, Q. Guo, B. Yang, J. H, Y. Bi, Y. Xiang, C. Liu, and S. Zhang, Observation of chiral zero mode in inhomogeneous three-dimensional Weyl metamaterials, Science **363**, 148 (2019).
[16] X. Huang, L. Zhao, Y. Long, P. Wang, D. Chen, Z. Yang, H. Liang, M. Xue, H. Weng, and Z. Fang, Observation of the chiral-anomaly-induced negative magnetoresistance in 3D Weyl semimetal TaAs, Phys. Rev. X **5**, 031023 (2015).
[17] L. Lu, J. D. Joannopoulos, and M. Soljačić, Topological photonics, Nat. Photonics **8**, 821 (2014).
[18] M. C. Rechtsman, J. M. Zeuner, A. Tünnermann, S. Nolte, M. Segev, and A. Szameit, Strain-induced pseudomagnetic field and photonic Landau levels in dielectric structures, Nat. Photonics **7**, 153 (2013).
[19] H. Abbaszadeh, A. Souslov, J. Paulose, H. Schomerus, and V. Vitelli, Sonic landau levels and synthetic gauge fields in mechanical metamaterials, Phys. Rev. Lett. **119**, 195502 (2017).
[20] X. Wen, C. Qiu, Y. Qi, L. Ye, M. Ke, F. Zhang, and Z. Liu, Acoustic Landau quantization and quantum-Hall-like edge states, Nat. Phys. **15**, 352 (2019).
[21] M. Yan, W. Deng, X. Huang, Y. Wu, Y. Yang, J. Lu, F. Li, and Z. Liu, Pseudomagnetic fields enabled manipulation of on-chip elastic waves, Phys. Rev. Lett. **127**, 136401 (2021).
[22] M. Wang, Q. Ma, S. Liu, R.-Y. Zhang, L. Zhang, M. Ke, Z. Liu, and C. T. Chan, Observation of boundary-induced chiral anomaly bulk states and their transport properties, Nat. Commun. **13**, 5916 (2022).
[23] H. R. Xia and M. Xiao, Reversal of the chiral anomaly bulk states with periodically staggered potential, Phys. Rev. B **107**, 035144 (2023).
[24] J. Lu, C. Qiu, M. Ke, and Z. Liu, Valley vortex states in sonic crystals, Phys. Rev. Lett. **116**, 093901 (2016).
[25] M. Wang, W. Zhou, L. Bi, C. Qiu, M. Ke, and Z. Liu, Valley-locked waveguide transport in acoustic heterostructures, Nat. Commun. **11**, 3000 (2020).
[26] Y. Yang, Y. Yamagami, X. Yu, P. Pitchappa, J. Webber, B. Zhang, M. Fujita, T. Nagatsuma, and R. Singh, Terahertz topological photonics for on-chip communication, Nat. Photonics **14**, 446 (2020).
[27] X. T. He, E. T. Liang, J. J. Yuan, H. Y. Qiu, X. D. Chen, F. L. Zhao, and J. W. Dong, A silicon-on-insulator slab for topological valley transport, Nat. Commun. **10**, 872 (2019).
[28] Y. Zeng, U. Chattopadhyay, B. Zhu, B. Qiang, J. Li, Y. Jin, L. Li, A. G. Davies, E. H. Linfield, B. Zhang, Y. Chong, and Q. J. Wang, Electrically pumped topological laser with valley edge modes, Nature (London) **578**, 246 (2020).
[29] A. B. Khanikaev, S. Hossein Mousavi, W. K. Tse, M. Kargarian, A. H. MacDonald, and G. Shvets, Photonic topological insulators, Nat. Mater. **12**, 233 (2013).

[30] A. B. Khanikaev and G. Shvets, Two-dimensional topological photonics, Nat. Photonics **11**, 763 (2017).
[31] K. Sun, A. Souslov, X. Mao, and T. C. Lubensky, Surface phonons, elastic response, and conformal invariance in twisted kagome lattices, Proc. Natl. Acad. Sci. U.S.A. **109**, 12369 (2012).
[32] H. Danawe, H. Li, K. Sun, and S. Tol, Finite-frequency topological maxwell modes in mechanical self-dual kagome lattices, Phys. Rev. Lett. **129**, 204302 (2022).
[33] P. Azizi, S. Sarkar, K. Sun, and S. Gonella, Dynamics of self-dual kagome metamaterials and the emergence of fragile topology, Phys. Rev. Lett. **130**, 156101 (2023).
[34] J. Ma, D. Zhou, K. Sun, X. Mao, and S. Gonella, Edge modes and asymmetric wave transport in topological lattices: Experimental characterization at finite frequencies, Phys. Rev. Lett. **121**, 094301 (2018).
[35] M. Fruchart, Y. Zhou, and V. Vitelli, Dualities and non-Abelian mechanics, Nature (London) **577**, 636 (2020).
[36] Q. Wu, H. Chen, X. Li, and G. Huang, In-plane second-order topologically protected states in elastic kagome lattices, Phys. Rev. Appl. **14**, 014084 (2020).
[37] H. Chen, H. Nassar, A. N. Norris, G. K. Hu, and G. L. Huang, Elastic quantum spin Hall effect in kagome lattices, Phys. Rev. B **98**, 094302 (2018).
[38] See Supplemental Material http://link.aps.org/supplemental/10.1103/PhysRevLett.132.086302 for how we distinguish between the in-plane mode and out-of-plane mode in elastic twisted kagome metamaterials, how fixed boundaries introduce CABSs in elastic twisted kagome metamaterials, the realization of free-boundary-induced CABSs in elastic wave phononic crystals with C_{6v} symmetry, the evolution of CABSs as the boundary changes, the influence of different boundary modifications on CABSs in elastic twisted kagome metamaterials, the mechanism of regulating CABSs by boundary potential, the effect of twist angle on the CABSs, the robustness of the CABSs against distortions, the complete valley conversion of CABSs, the on-chip tunable CABSs in nanomechanical lattices; and our methods, simulations, and experimental measurements, which includes Refs. [40–41].
[39] B. Graczykowski, M. Sledzinska, F. Alzina, J. Gomis-Bresco, J. S. Reparaz, M. R. Wagner, and C. S. Torres, Phonon dispersion in hypersonic two-dimensional phononic crystal membranes, Phys. Rev. B **91**, 075414 (2015).
[40] C. Lee, X. Wei, J. W. Kysar, and J. Hone, Measurement of the elastic properties and intrinsic strength of monolayer graphene, Science **321**, 385 (2008).
[41] W. Yuan, C. Yang, D. Zhang, Y. Long, Y. Pan, Z. Zhong, H. Chen, J. Zhao, and J. Ren, Observation of elastic spin with chiral meta-sources, Nat. Commun. **12**, 6954 (2021).
[42] D. Hatanaka, I. Mahboob, K. Onomitsu, and H. Yamaguchi, Phonon waveguides for electromechanical circuits, Nat. Nanotechnol. **9**, 520 (2014).
[43] X. Xi, J. Ma, S. Wan, C.-H. Dong, and X. Sun, Observation of chiral edge states in gapped nanomechanical graphene, Sci. Adv. **7**, eabe1398 (2021).
[44] J. Cha, K. W. Kim, and C. Daraio, Experimental realization of on-chip topological nanoelectromechanical metamaterials, Nature (London) **564**, 229 (2018).
[45] Q. H. Zhang, Y. Ying, Z. Z. Zhang, Z. J. Su, H. Ma, G. Q. Qin, X.-X. Song, and G. P. Guo, Graphene-based nanoelectromechanical periodic array with tunable frequency, Nano Lett. **21**, 8571 (2021).
[46] Z. D. Zhang, X. M. Zhang, S. Y. Yu, M. H. Lu, and Y. F. Chen, Tunable topological fano resonances in graphene-based nanomechanical lattices, Phys. Rev. Appl. **18**, 054029 (2022).
[47] M. Kurosu, D. Hatanaka, and H. Yamaguchi, Mechanical Kerr nonlinearity of wave propagation in an on-chip nanoelectromechanical waveguide, Phys. Rev. Appl. **13**, 014056 (2020).